Composition Homogeneity in InGaAs/GaAs Core–Shell Nanopillars Monolithically Grown on Silicon

Kar Wei Ng, Wai Son Ko, Roger Chen, Fanglu Lu, Thai-Truong D. Tran, Kun Li, and Connie J. Chang-Hasnain*

Department of Electrical Engineering and Computer Sciences, University of California at Berkeley, Berkeley, California 94720, United States

S *Supporting Information*

ABSTRACT: Alloy composition homogeneity plays an important role in the device performance of III−V heterostructures. In this work, we study the spatial composition uniformity of n-$In_{0.12}Ga_{0.88}As$/i-$In_{0.2}Ga_{0.8}As$/p-GaAs core−shell nanopillars monolithically grown on silicon. Cross sections extracted along the axial and radial directions are examined with transmission electron microscopy and energy-dispersive X-ray spectroscopy. Interestingly, indium-deficient segments with width ∼5 nm are observed to develop along the radial $\langle 11\bar{2}0 \rangle$ directions in the InGaAs layers. We attribute this spontaneous ordering to capillarity effect and difference in group-III adatom diffusion lengths. The slight fluctuation in indium content (∼4%), however, does not induce any noticeable misfit defects in the pure wurtzite-phased crystal. In contrast, the heterostructure exhibits excellent alloy composition uniformity along the axial [0001] direction. Furthermore, abrupt transitions of gallium and indium are seen at the heterointerfaces. These remarkable properties give rise to extraordinary optical performances. Lasing is achieved in the core−shell nanopillars upon optical pump despite the observed alloy composition fluctuation in the radial directions. The results here reveal the potential of the InGaAs-based core−shell heterostructures as efficient optoelectronic devices and high-speed heterojunction transistors directly integrated on silicon.

KEYWORDS: III−V nanopillar, laser, nanowire, core−shell, alloy ordering
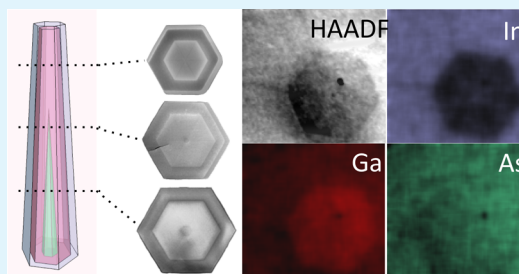
INTRODUCTION

III−V nanostructures synthesized on dissimilar substrates have shown great promise in the inexpensive integration of optoelectronics with many other possible functionalities.[1−4] Single-crystalline nanowires of diverse materials have been synthesized via vapor−liquid−solid (VLS) and selective area growth (SAG). When heterostructures in nanowires are used, various devices including light-emitting diodes,[5] high electron mobility transistors,[6] solar cells,[7] etc., have been demonstrated. While the small diameter can facilitate elastic strain relaxation and interesting quantum effects, the high surface-to-volume ratio increases the vulnerability of nanowires toward surface recombination. This can undesirably compromise the electrical and optical properties of the nanostructures.[8,9]

Recently, we reported a metastable core−shell growth mode that yields catalyst-free, high-quality (In)GaAs and InP nanoneedles and nanopillars on silicon.[10,11] With an unconventional stress-relaxing mechanism, these wurtzite-phased nanostructures can scale over a micrometer in base diameter while still maintaining excellent crystal quality, in spite of over 4% lattice mismatch with the substrate.[12] The large size effectively reduces the surface-to-volume ratio and enhances the optical confinement capability of the pillar natural cavity. Lasing of *as-grown* III−V pillars on silicon thus becomes possible.[11,13] Moreover, the core−shell geometry allows flexible heterostructure design with more tolerance toward lattice mismatch

than in conventional epitaxial growth.[14] Despite all the advantages in effective accommodation of lattice mismatch, we have very little understanding in the alloy composition uniformity in structures synthesized with this unique core−shell nanopillar growth mode. An inhomogeneity in alloy composition due to segregation or intermixing at interfaces can adversely impact the device performances. Therefore, a thorough compositional analysis, especially in the InGaAs/GaAs-based core−shell structure, is highly desirable.

In this paper, we study the alloy compositional coherence of a core−shell n-$In_{0.12}Ga_{0.88}As$/i-$In_{0.2}Ga_{0.8}As$/p-GaAs pillar, along both the axial and radial directions. With the use of high-angle annular dark field (HAADF) imaging and energy-dispersive X-ray spectroscopy (EDS), we analyze the spatial homogeneity of alloy compositions in the vertical and traverse cross sections of the nanostructure. Spontaneous alloy ordering is observed in the basal plane of the wurtzite-phased crystal. Specifically, indium-deficient segments develop along equivalent $\langle 11\bar{2}0 \rangle$ directions in the InGaAs layers. The composition fluctuation, however, is very small, to the point that it has no observable effect on the light emission properties of the nanostructure. On the other hand, indium and gallium exhibit abrupt transitions at
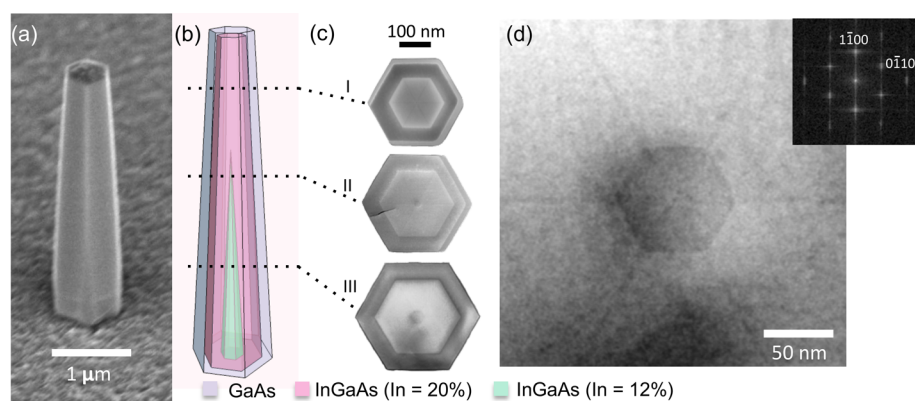
Figure 1. (a) SEM image of a typical as-grown $In_{0.12}Ga_{0.88}As/In_{0.2}Ga_{0.8}As/GaAs$ nanopillar grown on silicon. (b) Schematic diagram of the double heterostructure. (c) HAADF images of three traverse cross sections extracted from different locations of the pillar. Note that the innermost $In_{0.12}Ga_{0.88}As$ core shrinks and vanishes when moving up the pillar as a result of the characteristic core−shell growth. The crack in cross section II is an artifact induced during mechanical manipulation inside the FIB. (d) Magnified image of the central region of cross section III in (c). Inset shows the fast Fourier transform (FFT) of the lattice. The diametric lines are aligned to the $\langle 11\bar{2}0 \rangle$ directions.
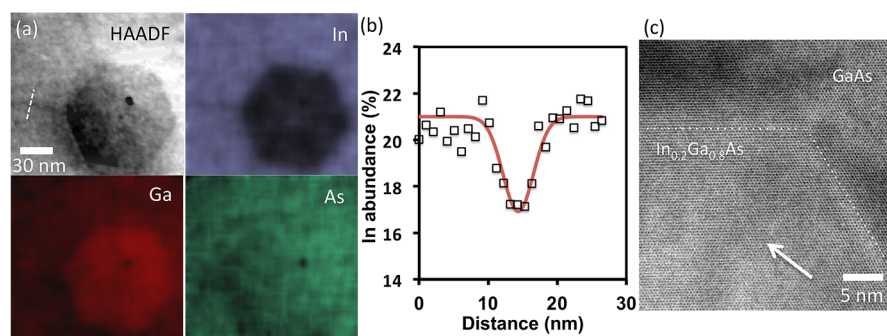

Figure 2. (a) Elemental maps of indium, gallium, and arsenic (152×152 sq. pixels). The indium map is an exact replica of the HAADF image, indicating that the diametric lines are indeed indium-deficient. (b) Line scan of indium across an indium-deficient line (indicated by a white dotted line in the HAADF image in (a)). With use of Gaussian fit, the minimum indium content and full-width at half-maximum are estimated to be 16.9% and 2.2 nm, respectively. (c) HAADF image showing a region close to the $In_{0.2}Ga_{0.8}As/GaAs$ interface (highlighted with dotted lines). The indium-deficient segment, indicated by an arrow, stretches out from the corner of the heterointerface.

the heterointerfaces, ensuring efficient carrier confinement within the active region. In addition, excellent uniformity in alloy composition is observed from the base to the tip of the nanostructure along [0001]. With the remarkable composition homogeneity and abrupt interfaces, lasing is achieved in the double heterostructure. This attests to the potential of the core−shell nano- and micropillars as efficient optoelectronic devices integrated monolithically on silicon.

■ SPONTANEOUS ORDERING ALONG THE RADIAL DIRECTION

Core−shell $In_{0.12}Ga_{0.88}As/In_{0.2}Ga_{0.8}As/GaAs$ nanopillars were grown on (111)-Si substrates in an Emcore D75 metalorganic chemical vapor deposition (MOCVD) reactor at 400 °C. Details of the growth can be found in our previous work.[13,15] Prior to the growth of the heterostructures, we calibrated the indium content by growing a series of bulk InGaAs pillars with various indium flow rates and deduced the indium compositions from their emission wavelengths. Notably, the $In_{0.12}Ga_{0.88}As$ core and GaAs shell are n- and p-doped with Te and Zn, respectively, with a dopant concentration of $\sim 10^{18}$ cm^{-3} in both cases. Figure 1a,b shows a scanning electron microscope (SEM) image of a typical as-grown nanopillar and its corresponding schematic. With a base diameter approaching 1 μm, the pillar resembles a hexagonal frustum with smooth,

well-faceted sidewalls. The $In_{0.2}Ga_{0.8}As$ active region is sandwiched between two larger bandgap materials for better carrier confinement and reduction of threshold current density for lasing. We note that the pillars exhibit respectable uniformity in base diameter, although the length may vary from pillar to pillar. This agrees with our observations in previous work.[13,16,17] With use of focused ion beam (FIB) and micromanipulator, thin slices of traverse cross sections were extracted from the nanostructures. The thin lamellas were examined with scanning transmission electron microscopy (STEM) for z-contrast analysis in a FEI-Titan operating at 300 kV (C_s = 1.2 mm) at the National Center for Electron Microscopy, Lawrence Berkeley National Laboratory. The STEM probe had a convergence semiangle α of 10 mrad. The STEM images were acquired using a Fischione HAADF detector with an inner semiangle β ranged from 61 to 79 mrad. Figure 1c displays HAADF-STEM images of three traverse cross sections cut at different locations of pillars. Since indium has a higher atomic number than gallium and arsenic, layers with more indium appear brighter in the z-contrast image. Cross section III consists of a three-layer architecture in which the innermost $In_{0.12}Ga_{0.88}As$ core is embedded within the $In_{0.2}Ga_{0.8}As$ active region and the GaAs shell. In particular, the three regions are completely concentric as a result of core−shell growth. In cross sections I and II, however, there exists an

asymmetric layer that wraps around the GaAs shell. Figure S1 in the Supporting Information shows that this nonconcentric layer is amorphous in nature, suggesting that it is an artifact due to ion beam damage during sample preparation and has no relation to the growth. When moving up from the base to the tip, one can notice that the innermost $In_{0.12}Ga_{0.88}As$ core shrinks in size and finally disappears in the topmost cross section. This is a direct consequence of the characteristic core−shell growth mode in which the $In_{0.12}Ga_{0.88}As$ core is completely embedded inside the active region in all growth directions. This observation agrees well with our core−shell model schematically illustrated in Figure 1b.

Another important feature observed in all three cross sections in Figure 1c is the diametric lines that spread out radially from the center of the hexagons. Figure 1d shows a magnified image of the central region of cross section III, which depicts an $In_{0.12}Ga_{0.88}As$ core surrounded by $In_{0.2}Ga_{0.8}As$. The faint dark lines start at the center, propagate through the $In_{0.12}Ga_{0.88}As$ and $In_{0.2}Ga_{0.8}As$ layers, and terminate at the $In_{0.12}Ga_{0.88}As$/GaAs interface. Specifically, the dark lines are extending along the equivalent $\langle 11\bar{2}0 \rangle$ directions and have a finite width of ~5 nm. The contrast observed suggests a deficiency in indium along the dark lines. EDS is utilized to analyze the composition variance over the area shown in Figure 1d. Inside the same microscope operating at 300 kV, X-ray signals were measured by an FEI Super-X Quad windowless detector based on silicon drift technology. We then used the Bruker ESPRIT software, which has been calibrated against mineral standards for quantitative accuracy, to process the spectra and generate elemental maps and line scans. The spatial distributions of indium, gallium, and arsenide are plotted out as elemental maps, as shown in Figure 2a. The corresponding HAADF image is also included in the same figure. The black dot at the center of the core is an artifact caused by electron beam damage during imaging. While arsenic shows a rather uniform distribution over the entire region, more gallium is detected in the core due to lower gallium content in the active region. The indium spatial map, on the other hand, is an exact replica of the HAADF image. Faint dark lines are observed to stretch out from the hexagonal $In_{0.12}Ga_{0.88}As$ core. An elemental line scan (Figure 2b) indicates that the indium content drops by ~4% across the indium-deficient line. This estimation is fairly consistent with the subtle contrast between the indium-deficient segment and the surrounding material in the HAADF image. A complementary behavior is also observed in the gallium line scan profile (not shown here). These observations reveal a spontaneous composition ordering of indium along the equivalent $\langle 11\bar{2}0 \rangle$ directions.

The observed natural alloy composition ordering can be attributed to capillarity effect that occurs during nonplanar growth. In wurtzite (WZ) nanostructures growing along the c-axis, sidewalls are usually composed of either m-planes (i.e., $\{1\bar{1}00\}$) or a-planes (i.e., $\{11\bar{2}0\}$). Experimentally, we observed that the pillar sidewalls are usually terminated with m-planes. This indicates that m-planes possess lower surface energy than a-planes under the pillar growth conditions, probably due to the high group III supply.[18] To minimize surface energy, $\{11\bar{2}0\}$ facets shrink into <10 nm in width. This leads to the formation of sharp corners in between adjacent $\{1\bar{1}00\}$ planes, as seen in the hexagonal cross sections in Figure 1. The sharp convex morphology promotes the diffusion of adatoms away from the sharp corners as a consequence of capillarity effect.[19,20] The longer diffusion length of indium adatoms

than gallium adatoms leads to a higher diffusion rate of indium from the $\{11\bar{2}0\}$ facets.[21] The unbalanced group III diffusions results in indium-deficient growth on the $\{11\bar{2}0\}$ facets and hence the diametric dark lines in the HAADF images. Notably, this is the first observation of orientation-specific ordering of indium in a pure wurtzite-phased nanostructure, to the best of our knowledge. A similar phenomenon is observed in GaAs/AlGaAs and GaAs/AlInP core−shell zinc-blende nano-wires.[22,23] In these nanostructures, Al-rich segments, segregating along the $\langle 112 \rangle$ directions, have lengths well below 100 nm. In our case, however, the indium-deficient growth along $\langle 11\bar{2}0 \rangle$ can stretch to over 400 nm in total length without causing any observable misfit defects. Figure 2c shows a corner where the diametric dark line terminates at the $In_{0.2}Ga_{0.8}As$/GaAs interface. Coherent honeycomb-like (0001) lattice continues seamlessly over all the regimes with different indium contents, revealing the single-crystalline nature of the nanostructure despite composition ordering.

Despite the occurrence of spontaneous ordering, excellent composition uniformity is observed along the radial direction. Figure 3a displays a portion of cross section III consisting of the
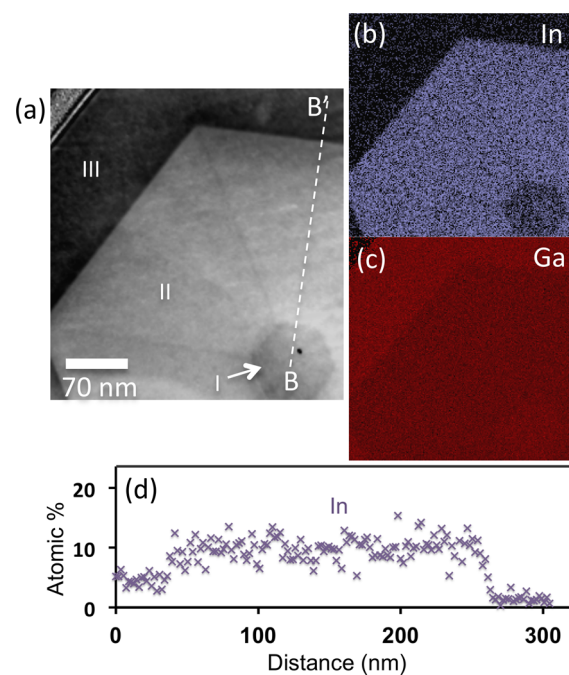

Figure 3. (a) HAADF image showing a traverse cross-section consisting of $In_{0.12}Ga_{0.88}As$ core (region I), $In_{0.2}Ga_{0.8}As$ active layer (region II) and GaAs shell (region III). The black dot inside the core is once again an electron "burn" mark. (b) Elemental map of indium. (c) Elemental map of gallium. (d) Elemental line scan of indium across B−B′. Indium shows very uniform distribution in each region and sharp transitions at the heterointerfaces. All maps are 196 × 208 sq. pixels in size.

entire three-layer heterostructure. The elemental maps in Figure 3b,c indicate that indium and gallium are very uniformly distributed over the whole active region, except for the indium-deficient lines that run along the $\langle 11\bar{2}0 \rangle$ directions. By scanning the electron beam across the line B−B′ indicated in Figure 3a, we obtained an elemental line scan of indium across all three regions in the heterostructure (see Figure 3d). Indium exhibits a very uniform profile in each of the three regions, as well as a sharp transition at each heterointerface. Such observation

confirms the alloy composition homogeneity of the active region along the radial directions, which is crucial to the optoelectronic performances of the nanostructure.

■ COMPOSITION HOMOGENEITY ALONG THE AXIAL DIRECTION

Composition coherence along the axial direction has profound impact on the light emission efficiency of the nanostructure. To study this, we cut through the center and examined the vertical cross section of the double heterostructure with HAADF imaging, as displayed in Figure 4a. A thick dark layer is
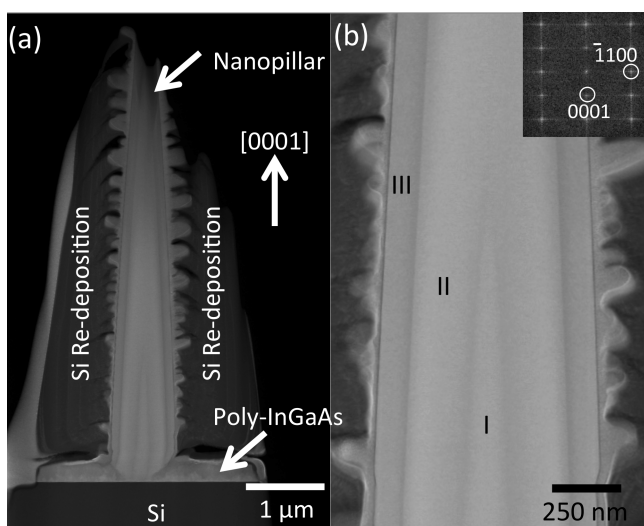

Figure 4. (a) z-Contrast image showing a vertical cross section of the double heterostructure. The dark layer embracing the nanopillar is ion-beam-induced redeposition of silicon created during TEM sample preparation. (b) Zoom-in view of the central region of (a). A three-layer architecture can be clearly seen. Regions I, II, and III are $In_{0.12}Ga_{0.88}As$, $In_{0.2}Ga_{0.8}As$, and GaAs, respectively. Inset is the FFT of the crystal lattice, taken along the a-axis.

observed to wrap around the nanopillar as a result of ion-beam-induced silicon redeposition formed during TEM sample preparation. The pillar cross section reveals a three-layer architecture, which can be seen more clearly in the magnified image in Figure 4b. We note that the vertical cross section

resembles exactly the core−shell structure schematic proposed in Figure 1b. Interestingly, the contrast difference between areas with different indium compositions is more subtle along $[11\bar{2}0]$ than $[0001]$ in Figure 1. This is due to the strong dependence of z-contrast imaging on crystal orientation. The effects of channeling and coherent scattering can vary significantly along different crystal directions, thus changing the relative contribution of Rutherford scattering (i.e., the mechanism that depends strongly on atomic number) to the signal detected at high angle.[24] We believe that Rutherford scattering is dominant along $[0001]$ much more than $[11\bar{2}0]$, hence leading to the subtle contrast in Figure 4. Inverse tapering is observed at the pillar base as a consequence of confined growth by the surrounding polycrystalline InGaAs layer.[12] Notably, the topmost 1 μm of the lamella appears darker because the top portion was more thinned down during top-down ion milling. In fact, the very tip of the pillar was completely removed during ion milling in spite of Pt passivation. In contrast, the bottom portion of the pillar shows rather even contrast along the vertical $[0001]$ direction, which is a first indication for uniform alloy composition along the axial direction.

The spatial distributions of indium, gallium, and arsenic in the vertical cross section are plotted out as elemental maps, as shown in Figure 5a. The corresponding HAADF image is also included in the same figure. To allow easier interpretation, we cropped away the signals obtained from the redeposition region. As expected, arsenic shows a fairly uniform distribution over the entire nanopillar since the III−V stoichiometry is independent of group III alloy composition. Indium and gallium, on the other hand, show a complementary behavior in distribution, as the two group III elements always add up to 50% of the total atomic abundance. Three regimes can be discerned in the indium and gallium maps, although the intensity contrast between $In_{0.12}Ga_{0.88}As$ and $In_{0.2}Ga_{0.8}As$ is a bit subtle to recognize. Interestingly, noticeable signal of indium is detected in the GaAs shell. We attribute this to the trace amount of indium that redeposits onto the lamella during ion milling. In fact, the measured average atomic abundance of indium is well below 0.5% in the shell region. Abrupt transitions of indium and gallium concentrations are observed across the heterointerfaces. The transition boundary can be thinner than 2 nm, consistent with our previous observation at
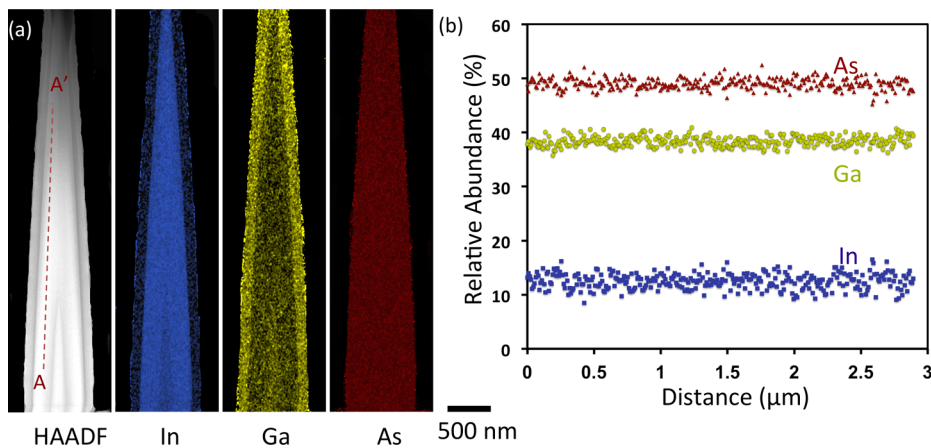

Figure 5. (a) Elemental maps of indium, gallium, and arsenic of the vertical cross section in Figure 4 (112 × 1024 sq. pixels). (b) Line scans of the three elements along A−A′ (see HAADF image in (a)). Indium and gallium show excellent uniformity over the entire length of 3 μm.

the InGaAs/GaAs interface in nanopillars grown on poly-Si.[25] Remarkably, the indium map shows fairly constant intensity over the entire $In_{0.2}Ga_{0.8}As$ active region, along the whole length of the pillar. To investigate the composition homogeneity more quantitatively, we performed a detailed elemental line scan along A−A′ (see the HAADF image in Figure 5a). As shown in Figure 5b, all three elements show very uniform profiles over the entire length of 3 μm. These results reveal the excellent composition uniformity of the active region along the axial direction, which is critical to the optical performance of the nanostructure.

LASING ACTION IN AS-GROWN NANOPILLARS

Photoluminescence is utilized to study the impact of the observed composition variances on the light emission properties of the nanostructure. Figure 6 displays the emission spectra
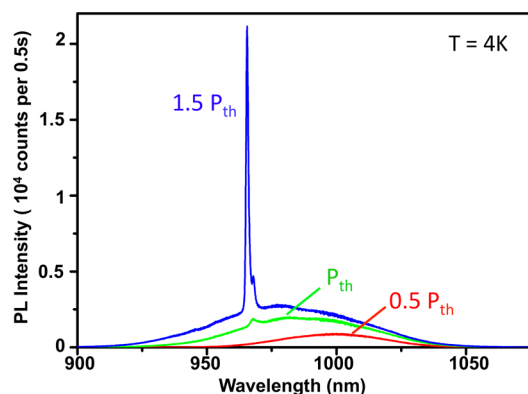

Figure 6. Emission spectra of an $In_{0.12}Ga_{0.88}As/In_{0.2}Ga_{0.8}As/GaAs$ nanopillar pumped at various powers. At 1.5 times threshold power, i.e., $1.5P_{th}$, a sideband suppression ratio of 10 dB is achieved. $P_{th} = 1$ mW.

of the double heterostructure pumped by a Ti:sapphire pulsed laser operating at 750 nm at 4 K. Under low pump power, only one single emission peak at ~1000 nm is observed, in spite of the presence of spontaneous alloy composition ordering along $\langle 11\bar{2}0 \rangle$. As the pump level increases, a cavity peak appears at 966 nm. The detuning between the gain and cavity resonance is probably due to the nonoptimized pillar dimensions and can be reduced by increasing the base diameter.[13] In spite of the gain-mode mismatch, lasing action can still be achieved at higher pump power. The extraordinary optical performance can be attributed to the excellent crystalline quality, abrupt heterostructure interfaces, and superior axial composition uniformity of the active region. Notably, we do not observe a significant wavelength shift or intensity drop in the emission from the heterostructure compared to the bulk pillars. We attribute this to the unique stress relaxing mechanism enabled by the extraordinary core−shell growth. As discussed in our previous work, the misfit strain relaxes elastically along the radial direction so that the misfit strain energy peaks at the heterointerfaces and drops quickly with the shell layer thickness.[14] We believe that most of the misfit strain (~0.5% between the core and active region) has relaxed elastically close to the heterointerfaces such that most of the 250 nm thick active region is almost free of stress. This is rather dissimilar to the conventional quantum wells in which the ~10 nm thick layer is fully stressed and the emission wavelength is highly sensitive to the strain condition. Although spontaneous alloy

ordering does occur along the radial directions, the mild indium fluctuation (~4%) in the narrow indium-deficient segments (~5 nm in width) causes no noticeable effect on the overall optical properties of the 1-μm-thick pillar. This is quite different from GaAs−AlGaAs core−shell nanowires in which the Al composition can go up by almost 30% in the Al-rich segments.[23] The high Al content can result in deep level traps which can adversely affect the optoelectronic performance of the nanowires.[26] In addition, it is particularly remarkable that the excellent optical properties of the heterostructured pillars are not negatively impacted by the introduction of dopants, which can lead to undesirable effects like free carrier absorption and formation of irradiative recombination centers. Compared to the simple undoped $In_{0.2}Ga_{0.8}As/GaAs$ core−shell pillar examined in ref 12, the realization of high-quality heterostructures with proper doping design not only represents a big step forward toward practical optical devices but also opens up new possibilities for other applications like high-speed heterobipolar junction transistors. In fact, high-speed photodetectors and emitters showing prominent amplified spontaneous emissions have been demonstrated with the core−shell pillars grown directly on silicon.[15] These promising results indicate the potential of the heterostructured pillars for the monolithic integration of efficient optoelectronic devices and high-speed heterojunction transistors with silicon.

CONCLUSIONS

In summary, we studied the alloy composition homogeneity of core−shell $In_{0.12}Ga_{0.88}As/In_{0.2}Ga_{0.8}As/GaAs$ pillars. Narrow indium-deficient segments are found to develop along $\langle 11\bar{2}0 \rangle$ spontaneously as a result of capillarity effect and difference in adatom mobilities. The indium drop is only ~4% and no misfit defects associated with the spontaneous alloy composition ordering are observed. On the other hand, excellent composition uniformity is observed in the $In_{0.2}Ga_{0.8}As$ active region along the entire length of the pillar. Lasing is achieved in the double heterostructure upon optical pump. The extraordinary optical performance indicates that the slight indium fluctuation along $\langle 11\bar{2}0 \rangle$ presents no noticeable effect on the optical properties and the superior alloy composition homogeneity enables efficient light emission from the entire length of the nanopillar.

ASSOCIATED CONTENT

Ⓢ Supporting Information
High-resolution HAADF-STEM image showing the amorphous nature of the artifact layer in Figure 1c. This material is available free of charge via the Internet at http://pubs.acs.org.

AUTHOR INFORMATION

Corresponding Author
*E-mail: cch@berkeley.edu.
Notes
The authors declare no competing financial interest.

ACKNOWLEDGMENTS

■ REFERENCES

(1) Munshi, A. M.; Dheeraj, D. L.; Fauske, V. T.; Kim, D. C.; van Helvoort, A. T. J.; Fimland, B.; Weman, H. Vertically Aligned GaAs Nanowires on Graphite and Few-Layer Graphene: Generic Model and Epitaxial Growth. *Nano Lett.* **2012**, *12* (9), 4570−4576.

(2) Lu, F.; Tran, T. T. D.; Ko, W. S.; Ng, K. W.; Chen, R.; Chang-Hasnain, C. J. Nanolasers Grown on Silicon-based MOSFETs. *Opt. Express* **2012**, *20*, 12171−12176.

(3) Dhaka, V.; Haggren, T.; Jussila, H.; Jiang, H.; Kauppinen, E.; Huhtio, T.; Sopanen, M.; Lipsanen, H. High Quality GaAs Nanowires Grown on Glass Substrates. *Nano Lett.* **2012**, *12*, 1912−1918.

(4) Ikejiri, K.; Ishizaka, F.; Tomioka, K.; Fukui, T. GaAs Nanowire Growth on Polycrystalline Silicon Thin Films using Selective-area MOVPE. *Nanotechnology* **2013**, *24*, 115304.

(5) Svensson, C. P. T.; Mårtensson, T.; Trägårdh, J.; Larsson, C.; Rask, M.; Hessman, D.; Samuelson, L.; Ohlsson, J. Monolithic GaAs/InGaP Nanowire Light Emitting Diodes on Silicon. *Nanotechnology* **2008**, *19*, 305201.

(6) Li, Y.; Xiang, J.; Qian, F.; Gradecak, S.; Wu, Y.; Yan, H.; Blom, D. a; Lieber, C. M. Dopant-free GaN/AlN/AlGaN Radial Nanowire Heterostructures as High Electron Mobility Transistors. *Nano Lett.* **2006**, *6*, 1468−73.

(7) Krogstrup, P.; Jørgensen, H. I.; Heiss, M.; Demichel, O.; Holm, J. V.; Aagesen, M.; Nygard, J.; Morral, A. F. i. Single-Nanowire Solar Cells beyond the Shockley−Queisser Limit. *Nat. Photonics* **2013**, *7*, 306−310.

(8) Dan, Y.; Seo, K.; Takei, K.; Meza, J. H.; Javey, A.; Crozier, K. B. Dramatic Reduction of Surface Recombination by in Situ Surface Passivation of Silicon Nanowires. *Nano Lett.* **2011**, *11*, 2527−2532.

(9) Chang, C. C.; Chi, C. Y.; Yao, M.; Huang, N.; Chen, C. C.; Theiss, J.; Bushmaker, A. W.; LaLumondiere, S.; Yeh, T. W.; Povinelli, M. L.; Zhou, C.; Dapkus, P. D.; Cronin, S. B. Electrical and Optical Characterization of Surface Passivation in GaAs Nanowires. *Nano Lett.* **2012**, *12* (9), 4484−4489.

(10) Moewe, M.; Chuang, L. C.; Crankshaw, S.; Chase, C.; Chang-Hasnain, C. J. Atomically Sharp Catalyst-Free Wurtzite GaAs/AlGaAs Nanoneedles Grown on Silicon. *Appl. Phys. Lett.* **2008**, *93*, 23116.

(11) Ren, F.; Ng, K. W.; Li, K.; Sun, H.; Chang-Hasnain, C. J. High-Quality InP Nanoneedles Grown on Silicon. *Appl. Phys. Lett.* **2013**, *102*, 012115.

(12) Ng, K. W.; Ko, W. S.; Tran, T. T. D.; Chen, R.; Nazarenko, M. V.; Lu, F.; Dubrovskii, V. G.; Kamp, M.; Forchel, A.; Chang-Hasnain, C. J. Unconventional Growth Mechanism for Monolithic Integration of III−V on Silicon. *ACS Nano* **2013**, *7*, 100−107.

(13) Chen, R.; Tran, T. T. D.; Ng, K. W.; Ko, W. S.; Chuang, L. C.; Sedgwick, F. G.; Chang-Hasnain, C. J. Nanolasers Grown on Silicon. *Nat. Photonics* **2011**, *5*, 170−175.

(14) Nazarenko, M. V.; Sibirev, N. V.; Ng, K. W.; Ren, F.; Ko, W. S.; Dubrovskii, V. G.; Chang-Hasnain, C. J. Elastic Energy Relaxation and Critical Thickness for Plastic Deformation in the Core−Shell InGaAs/GaAs Nanopillars. *J. Appl. Phys.* **2013**, *113*, 104311.

(15) Chen, R.; Ng, K. W.; Ko, W. S.; Parekh, D.; Lu, F.; Tran, T. T. D.; Li, K.; Chang-Hasnain, C. J. Nanophotonic Integrated Circuits Assembled from Nanoresonators Grown on Silicon. *Nat. Commun.* **2014**, *5*, 4325.

(16) Ng, K. W.; Ko, W. S.; Lu, F.; Chang-Hasnain, C. J. Metastable Growth of Pure Wurtzite InGaAs Microstructures. *Nano Lett.* **2014**, *1*, 1.

(17) Chuang, L. C.; Sedgwick, F. G.; Chen, R.; Ko, W. S.; Moewe, M.; Ng, K. W.; Tran, T. T. D.; Chang-Hasnain, C. J. GaAs-Based Nanoneedle Light Emitting Diode and Avalanche Photodiode Monolithically Integrated on a Silicon Substrate. *Nano Lett.* **2011**, *11*, 385−390.

(18) Yamashita, T.; Akiyama, T.; Nakamura, K.; Ito, T. Growth of Side facets in InP Nanowires: First-Principles-Based Approach. *Surf. Sci.* **2013**, *609*, 207−214.

(19) Biasiol, G.; Gustafsson, a.; Leifer, K.; Kapon, E. Mechanisms of Self-ordering in Nonplanar Epitaxy of Semiconductor Nanostructures. *Phys. Rev. B* **2002**, *65*, 1−15.

(20) Wagner, J. B.; Sköld, N.; Reine Wallenberg, L.; Samuelson, L. Growth and Segregation of GaAs−Al$_x$In$_{1−x}$P Core-Shell Nanowires. *J. Cryst. Growth* **2010**, *312*, 1755−1760.

(21) Kim, Y.; Joyce, H. J.; Gao, Q.; Tan, H. H.; Jagadish, C.; Paladugu, M.; Zou, J.; Suvorova, A. A. Influence of Nanowire Density on the Shape and Optical Properties of Ternary InGaAs Nanowires. *Nano Lett.* **2006**, *6* (4), 599−604.

(22) Fickenscher, M.; Shi, T.; Jackson, H. E.; Smith, L. M.; Yarrison-Rice, J. M.; Zheng, C.; Miller, P.; Etheridge, J.; Wong, B. M.; Gao, Q.; Deshpande, S.; Tan, H. H.; Jagadish, C. Optical, Structural, and Numerical Investigations of GaAs/AlGaAs Core-multishell Nanowire Quantum Well Tubes. *Nano Lett.* **2013**, *13*, 1016−1022.

(23) Rudolph, D.; Funk, S.; Döblinger, M.; Morkötter, S.; Hertenberger, S.; Schweickert, L.; Becker, J.; Matich, S.; Bichler, M.; Spirkoska, D.; Zardo, I.; Finley, J. J.; Abstreiter, G.; Koblmüller, G. Spontaneous Alloy Composition Ordering in GaAs−AlGaAs Core−Shell Nanowires. *Nano Lett.* **2013**, *13*, 1522−1527.

(24) Pennycook, S. J. Z-contrast STEM for Materials Science. *Ultramicroscopy* **1989**, *30*, 58−69.

(25) Ng, K. W.; Tran, T. T. D.; Ko, W. S.; Chen, R.; Lu, F.; Chang-Hasnain, C. J. Single Crystalline InGaAs Nanopillar Grown on Polysilicon with Dimensions beyond the Substrates Grain Size Limit. *Nano Lett.* **2013**, *13*, 5931−5937.

(26) Bourgoin, J. C. Physics of DX Centers in GaAs and Alloy. *Solid State Phenom.* **1991**, 10.